Modeling and Control of a Bioinspired, Distributed Electromechanical Actuator System Emulating a Biological Spine

Bonhyun Ku, *Student Member, IEEE*, and Arijit Banerjee, *Senior Member, IEEE*

***Abstract*—The robotic spine has a lot of potential for snake-like, quadruped, and humanoid robots, as it can improve their mobility, flexibility, and overall function. A common approach to developing an articulated spine uses geared motors to imitate vertebrae. Instead of using geared motors that rotate 360 degree, a bioinspired gearless electromechanical actuator was proposed and developed as an alternative, specifically for humanoid spine applications. The actuator trades off angular flexibility for torque, while the geared motor trades off speed for torque. This article compares the proposed actuator and conventional geared motors regarding torque, acceleration, and copper loss for a vertebra's angular flexibility. When its angular flexibility is lower than 14°, the proposed actuator achieves higher torque capability without gears than with conventional motors. Lower angular flexibility, which means smaller airgaps, allows the proposed actuator to produce a much stronger torque for the same input power. The actuator's nonlinear electrical and mechanical dynamics models are developed and used for position control of a six-module distributed spine. In addition, two different position-control architectures are developed: an outer loop proportional-integral (PI) position controller with an inner loop PI current controller and an outer loop PI position controller with an inner loop PI torque controller.**

***Index Terms*—Bioinspired actuator, distributed actuator, gearless actuator, robotic spine.**

I. INTRODUCTION

THE spine, along with its muscular system, is an example of a distributed actuation mechanism in animals. It provides energy-efficient locomotion [1] and allows dynamic, flexible, and balanced motions in vertebrates [2], [3], [4], [5], [6], [7]. Attempts have been made to incorporate an articulated spine in bio-inspired robots to increase the range of motion and performance [8], [9], [10]. Actuators used to create these synthetic spines include tendon-driven [5], [11], [12], [13], cable-driven [14], [15], and geared electric motors [16], [17], [18]. This article focuses on creating a synthetic spine using a new class of distributed electromechanical actuators.

Intrinsically, electrical power is the driving source in all of the existing synthetic spine actuation mechanisms, with an electric motor somewhere in the energy-processing path. For example, tendon-driven or cable-driven actuators use an electric motor to transmit the motion to the joint via a flexible link [19]. While this mechanism mimics the natural motion of muscles and tendons, adding flexibility and compliance, precise control is challenging as the flexible link is prone to stretch [20]. Robots, such as Kenshiro [5], Kenta [11], and Kengoro [12] lack human agility, suggesting that these mechanisms' control bandwidth is limited. Similarly, state-of-the-art cable-driven continuum robots have been developed with motor-based actuation [21], [22], [23]. However, cable-driven continuum robots have separate mechanical structures and actuation, resulting in a bulky and complex system design using multiple geared motors with cables [24], [25]. Tendon-driven [26], [27] and cable-driven [28] exoskeletons supporting the trunk also utilize geared motors.

Brushless dc (BLDC) motors with gears are most commonly used to create articulated spine applications. For example, the Carnegie Mellon University (CMU) snake robot [16], the salamander robot [17], and Bobcat [18] have been developed based on axial-driven actuation using geared motors. A waist-trunk system with parallel manipulators performed lateral-bending and transverse-rotation movements using motors [29]. In addition, the quadruped robot MIT Cheetah [14], Transleg [30], Robotic Rat [7], and humanoid spines [5], [11], [12], [31], [32], [33], [34], [35] have been developed with cable-driven geared motors for the distributed actuation of their spines. Geared electric motors trade speed for torque, which leads to poor back-drivability—the ability for bidirectional interactive force transmission between the actuator and its environment [36]. Mechanical springs between the motor and end effector are often used to add compliance [37], [38]. Complex mechanical fixtures and multiple parts are required to adopt a 360-degree motion space to achieve a distributed actuation with limited displacement [39]. Replacing conventional gears with a harmonic

Manuscript received 24 March 2023; revised 29 November 2023 and 15 April 2024; accepted 27 May 2024. Recommended by Technical Editor G. Carbone and Senior Editor S. Katsura. This work was supported by National Science Foundation under Grant 1943791. *(Corresponding author: Bonhyun Ku.)*

The authors are with the Department of Electrical and Computer Engineering, University of Illinois at Urbana-Champaign, Urbana, IL 61801 USA (e-mail: bonhyun.k@gmail.com, bonhyun2@illinois.edu; arijit@illinois.edu).

This article has supplementary material provided by the authors and color versions of one or more figures available at https://doi.org/10.1109/TMECH.2024.3409696.

Digital Object Identifier 10.1109/TMECH.2024.3409696

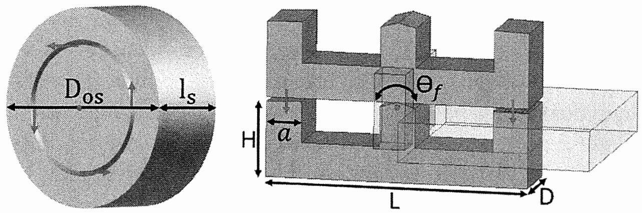

(a) (b)

Fig. 3. Conventional motor uses tangential force while the proposed actuator utilizes normal force with limited rotation. (a) Conventional motor. (b) Proposed actuator.

can be extended for quadruped robots with additional design considerations to counteract gravity.

II. COMPARISONS TO CONVENTIONAL MOTORS

At the microscopic level, a conventional motor utilizes tangential force to produce rotational motion, i.e., it relies on shear stress, as shown in Fig. 3(a). Using Maxwell's stress tensor, the shear stress can be expressed as [47]

$$f_t = \frac{B_n B_t}{\mu_0} \tag{1}$$

where B_t is the tangential flux density, B_n is the normal flux density, and μ_0 is the permeability of free space.

In theory, the normal flux density must be within the saturation flux density of the magnetic material while the tangential flux density is determined by the current density limit. In sub-kW motors with dimensions in tens of centimeters and a mass of a few hundred grams—a typical range for robotic actuators—the feasible average shear stress is on the order of tens of kPa [48]. Intuitively, this low shear stress is attributed to a lower practical limit on B_t and challenges in removing heat from a small volume [49]. This fundamental limit restricts the capability to construct a direct-drive, high-torque-density robotic actuator.

In comparison, the proposed actuator utilizes normal forces to produce motion, as shown in Fig. 3(b). The magnetic field in the gap is predominantly in the normal direction with a negligible tangential component. Normal stress can be expressed as [47]

$$f_n = \frac{B_n^2 - B_t^2}{2\mu_0}. \tag{2}$$

The negative sign in (2) is from the electromagnetic force on the charges in a volume [50]. Theoretically, assuming even a modest normal airgap flux density of 1 T, again limited by the magnetic material, allows a theoretical limit of 400 kPa, giving headroom to increase the motion-producing stress by 10×. To put this limit in a bioinspiration perspective, typical specific tension in skeletal muscles of vertebrates ranges from around 200–300 kPa [51]. In practice, the absolute torque density is dependent on many factors, including the area over which this stress is acting as well as on other second-order effects. The following sections delve further into these effects to better quantify the advantages of the proposed actuation mechanism from torque density, copper loss, and dynamic performance perspectives.

A. Torque Capability of Conventional Motors

The torque produced by a conventional motor is [49]

$$\tau_m = \underbrace{\frac{\sqrt{2}\pi}{16}\eta\cos\phi\left[a_r\left(\frac{D_{\text{is}}}{D_{\text{os}}}\right)^3 - 2b_r\left(\frac{D_{\text{is}}}{D_{\text{os}}}\right)^2 + \frac{D_{\text{is}}}{D_{\text{os}}}\right]}_{G_m} \times k_{\text{cu}}(D_{\text{os}}^3 l_s)(B_{g1}J_s) \tag{3}$$

where D_{is} is the inner stator diameter, D_{os} is the outer stator diameter, l_s is the motor stator length, B_{g1} is the peak fundamental component of air-gap flux density, k_{cu} is the copper winding fill factor, η is the efficiency, $\cos\phi$ is the power factor, and J_s is the slot current density. a_r and b_r are constants dependent on the air gap-to-tooth and air gap-to-core flux density ratios. Denoting G_m as the motor torque coefficient, this expression relates the torque capability of an electric motor to external dimensions, air-gap flux density limit, and current density limit.

B. Torque Capability of the Proposed Actuator

The next step is to derive a similar expression for the proposed actuator. Neglecting the core reluctance, the air-gap flux density is given by [44]

$$B_g = \frac{\mu_0 N I}{g_{\text{nom}}} \tag{4}$$

where N is the number of coil turns, I is the coil current, and g_{nom} is the nominal air-gap distance. g_{nom} is a key parameter of the proposed actuator determining the angular flexibility of individual modules. g_{nom} is related to the module length L and angular flexibility θ_f, as shown in Fig. 3, by [52]

$$g_{\text{nom}} = L\tan\frac{\theta_f}{4}. \tag{5}$$

The effective current density is expressed as

$$J_{\text{coil}} = \frac{2NI}{k_{\text{cu}}(L-3a)(L-a)} \tag{6}$$

where k_{cu} is the copper-winding fill factor and a is the module core limb width. Using (2), the normal stress of the proposed actuator is given by

$$f_{\text{actuator}} = \frac{B_g^2}{2\mu_0} = \frac{k_{\text{cu}}(L-3a)(L-a)}{4L\tan\frac{\theta_f}{4}}(B_g J_{\text{coil}}). \tag{7}$$

Multiplying the normal stress with the force-producing area ($A_c = aD$) and moment-arm length (r) results in the torque capability of the proposed actuator. Approximating the moment-arm length as

$$r = \frac{L-a}{2} \tag{8}$$

the proposed actuator's torque capability is

$$\tau_a = \underbrace{\frac{1}{8\tan(\theta_f/4)}\left[\left(\frac{a}{L}\right)\left(1-\frac{3a}{L}\right)\left(1-\frac{a}{L}\right)^2\right]}_{G_a} \times k_{\text{cu}}(DL^3)(B_g J_{\text{coil}}) \tag{9}$$

TABLE I
PROPOSED ACTUATORS ARE DESIGNED FOR MAXIMUM SPECIFIC TORQUE AT NOMINAL POSITION (0°) WITH VARIOUS VOLUME CONSTRAINTS AND BENDING-ANGLE TARGETS

Distributed actuator	Spine bending angle [deg]	Module number	θ_f [deg]	L [mm]	H [mm]	D [mm]	Module weight [kg]	Module inertia [kgm^2]	Module torque at 0 deg [N·m]	Normal stress at 0 deg [kPa]
P1 [45]	18	6	9	50.0	40.0	10.0	0.310	0.0003149	0.5	250
P2	10	10	4	60.0	18.3	12.7	0.283	0.0002368	1.34	592.1
P3	10	10	4	76.0	22.8	17.1	0.553	0.0006971	4.07	789.5
P4	10	10	4	86.0	26.0	18.7	0.819	0.0013690	7.77	1113
P5 [53]	10	10	4	101	28.3	24.7	1.120	0.0020598	11.3	753.5
P6	5	10	2	63.0	18.6	16.4	0.300	0.0002207	4.95	1282
P7	5	10	2	79.0	23.2	20.8	0.587	0.0006695	12.8	1642
P8	5	10	2	91.0	26.4	22.4	0.819	0.0012080	19.6	1712
P9	5	10	2	103	29.1	22.7	1.039	0.0019296	26.4	1729

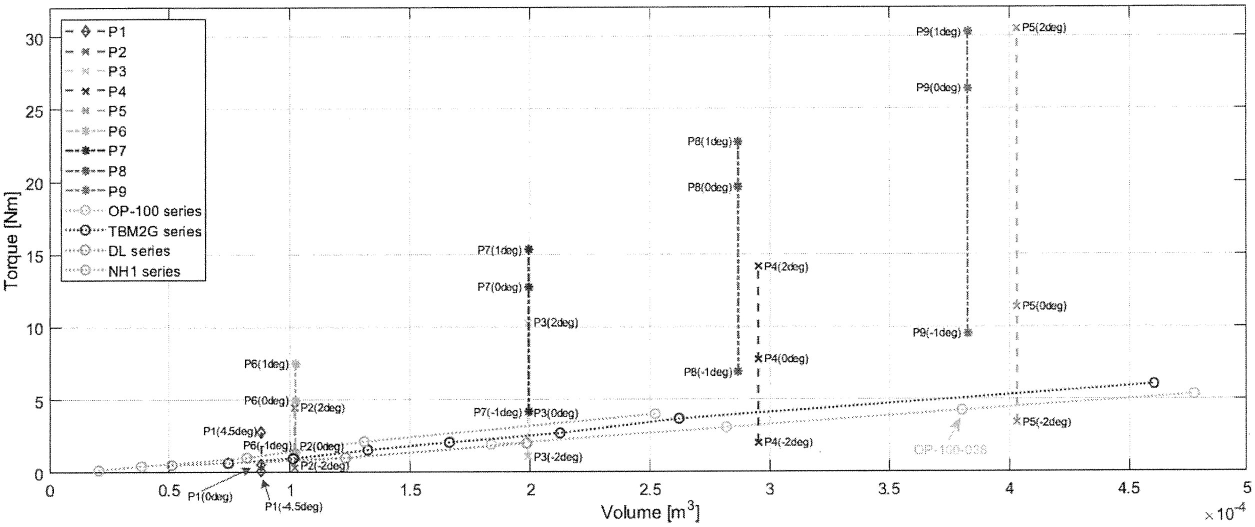

Fig. 5. Torque capability of the proposed actuators with limited angular flexibility outperforms conventional BLDC motors used in robotics.

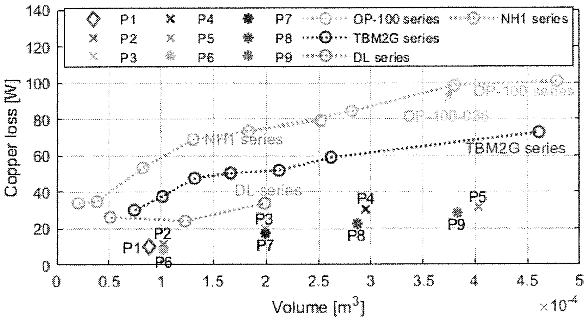

Fig. 6. Proposed actuator copper loss is significantly lower than conventional motors for the same volume.

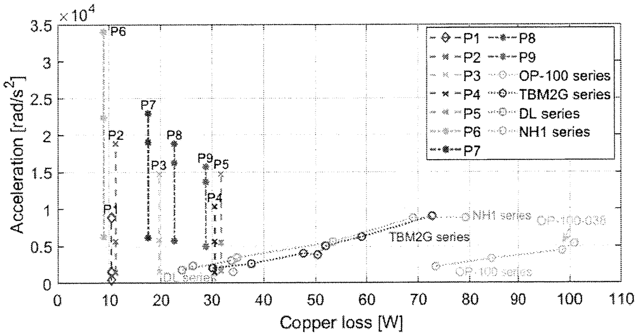

Fig. 7. Dynamic performance of the geared motors and the proposed actuators are compared for copper loss.

conventional motors to match the torque capability of module P5 at 0°. Gear inertia and efficiency are ignored. The reflected inertia of the rotor for each motor is used to calculate instantaneous acceleration without friction from the torque with gears as

$$\tau = G^2 J_{\text{motor}} \ddot{\theta}_{\text{motor}} \tag{10}$$

where G is the gear ratio. For the proposed actuator, the module inertia in Table I without gears is used

$$\tau = J_{\text{actuator}} \ddot{\theta}_{\text{actuator}}. \tag{11}$$

Accelerations of the geared motors and the gearless proposed actuators are plotted relative to the copper losses for an identical torque capability, as shown in Fig. 7. The proposed actuators

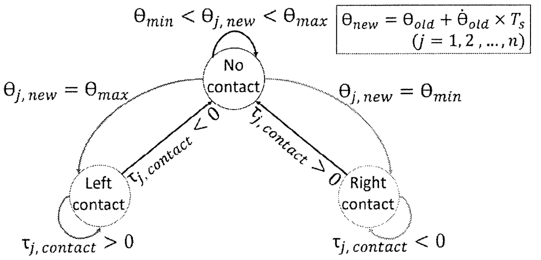

Fig. 8. Contact-state flow chart of the distributed spine. There are three contact states for a module: no contact, left contact, and right contact. T_s is the sampling time step.

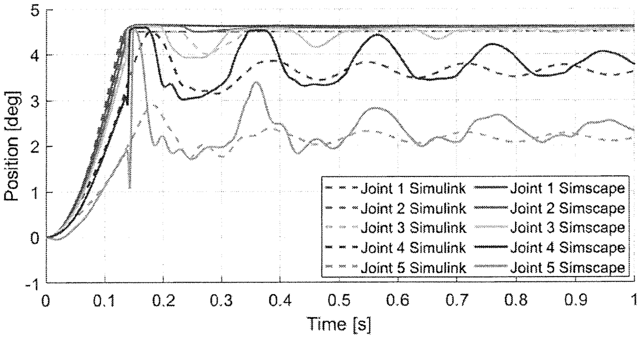

Fig. 9. Simulink spine dynamics with contact model matches well with the Simscape model regarding position changes, contacts, and damping when constant torques are applied.

based on the joint acceleration, velocity, previous position, and time step. If the new position exceeds the allowable range of motion, the module state changes to a contact state. Alternatively, if a module is in a contact state, the contact torque sign determines if the module remains in contact or comes out of contact. For example, if a module is in contact at the maximum position, the module will remain in contact if the contact torque is still positive. Conversely, when the contact torque becomes negative, the module will be released from the contact state. This approach inherently assumes inelastic contact collisions between modules.

To verify the mechanical model of the distributed spine with contacts, (14) is modeled in MATLAB Simulink for a 5-link distributed spine. Model parameters are listed in [46]. As a benchmark, a MATLAB Simscape model is also constructed using assembled computer aided design (CAD) models of actual modules considering distributed mass. The Simscape model uses an elastic contact model.

A constant torque at each joint ($\tau_e = [0.5751, 0.4224, 0.2748, 0.1434, 0.0445]^T$ N · m) is applied to both the Simulink as well as the Simscape models. Higher torques applied to lower joints are selected, as stiffer springs are used at lower joints. Fig. 9 shows that the analytical model in Simulink matches the Simscape model reasonably well. The Simulink model captures the contact-state flow for Joints 3 and 4. Joints 1 through 3 settle at a contact state, while Joints 4 and 5 settle at a position where the equilibrium happens with the spring and gravitational torques. The discrepancies between the two responses can be attributed to the mass matrix approximation, the assumption on $c(\theta, \dot{\theta})$, and differences in contact modeling. Nevertheless, the ability to model the mechanical dynamics in Simulink reduces the simulation time from tens of minutes (if the Simscape model is used) to a few seconds, enabling the exploration of various control architectures and comparing their performance in a reasonable time.

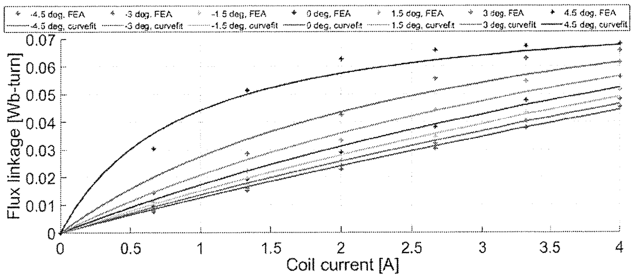

Fig. 10. Flux linkage is a highly nonlinear function of the joint position and coil current. The flux linkage of the actuator is modeled by adapting the Fröhlich model.

B. Modeling the Electrical Dynamics

Unlike conventional motors, the electrical dynamics of the proposed actuator is a nonlinear function of position and coil current. The system's nonlinear behavior becomes more pronounced due to the saturation of the magnetic core and the fringing effect in the airgap [57]. A flux-linkage model with respect to position and coil current is necessary to create the nonlinear electrical model. Fröhlich proposed a curve-fitting approach to capture the nonlinearity in B–H curves of magnetic materials [58], [59]

$$B = \frac{\alpha H}{\beta + H} \tag{15}$$

where α and β are positive constants.

Adapting Fröhlich's model to account for different air-gap distances (related to joint position), the flux linkage for one coil in a module can be expressed as

$$\lambda(\theta, i) = \frac{\alpha(\theta) i}{\beta(\theta) + i} \tag{16}$$

where $\alpha(\theta) = \alpha_1\theta^2 + \alpha_2\theta + \alpha_3$, $\beta(\theta) = \beta_1\theta^2 + \beta_2\theta + \beta_3$, and i is the coil current. The second-order polynomial equations $\alpha(\theta)$ and $\beta(\theta)$ represent flux-linkage changes based on position, similar to a switched-reluctance motor [57]. A finite element analysis (FEA)-based magnetostatic model of one module is developed in ANSYS Maxwell to calculate the coefficients in (16). Fig. 10 shows the flux linkage of the magnetostatic model for different joint angles and current excitation and the corresponding approximate curves capturing the nonlinearity. The coefficients used in Fig. 10 are $[\alpha_1, \alpha_2, \alpha_3] = [2.5242, -1.1867, 0.1599]$ and $[\beta_1, \beta_2, \beta_3] = [375.9, -123.4, 8.234]$. Therefore, the electrical

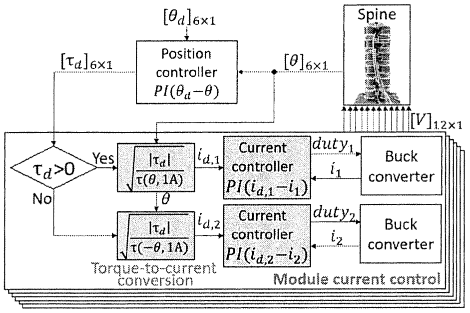

Fig. 13. PI position controller with inner loop PI current controller. A lookup table is used for torque-to-current conversion.

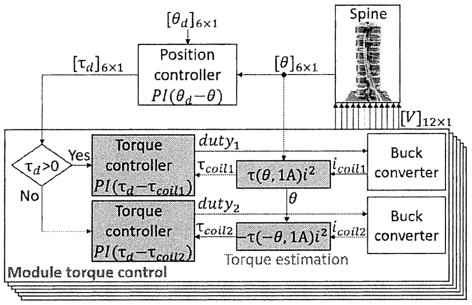

Fig. 14. PI position controller with inner loop PI torque controller. Torque is estimated using the normalized torque lookup table.

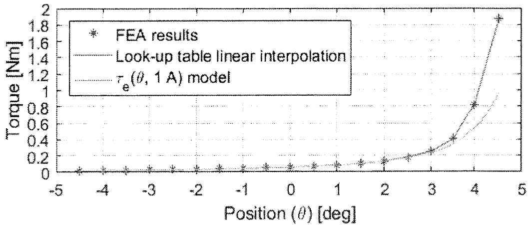

Fig. 15. Normalized torque at 1 A coil current for a left coil look-up table is used for torque-to-current conversion.

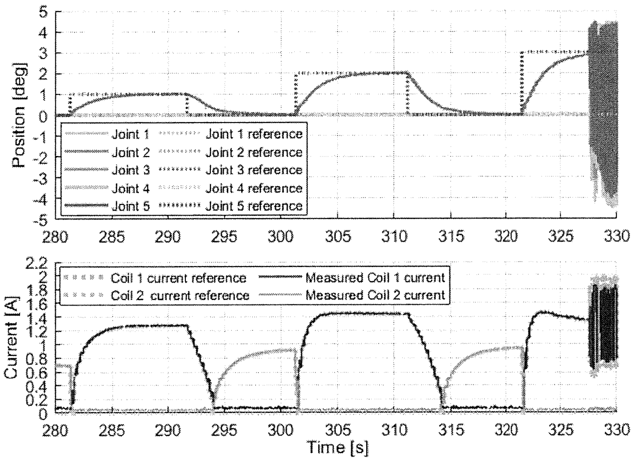

Fig. 16. Experimental results: The position control with the inner loop current controller.

controller with an inner loop PI *current* controller is used. In the second architecture, shown in Fig. 14, an outer loop PI position controller with an inner loop PI *torque* controller is used.

A. Nonlinear Relationship Between Torque and Current

Unlike in conventional motors, the torque-current relationship in the proposed actuator is nonlinear and is dependent on the actuator position, as observed in (19), making it challenging from a real-time computation perspective for closed-loop position control. Instead, a lookup table is developed to calculate the coefficient that relates the torque to the square of the coil current, thereby reducing the real-time computational complexity [46]. In this simplified form, the torque-to-current relationship is

$$|\tau_e| = \tau_{\text{lookup}}(\theta, 1\,\text{A}) \times i_{\text{coil}}^2 \qquad (20)$$

where $\tau_{\text{lookup}}(\theta, 1\,\text{A})$ is the lookup table output for different positions with a coil current of 1 A. While (19) can be used to generate this table, we created one using an FEA model of the actuator in ANSYS Maxwell, as shown in Fig. 15, for better accuracy, particularly at smaller gaps. Linear interpolation is used between data points for practical implementation.

B. Control Architecture With Inner Loop PI Current Controller

An outer loop PI controller determines the desired torque based on the position error at individual joints, as shown in Fig. 13. Depending on the polarity of the desired torque, the right or the left coil is commanded. The lookup table calculates the desired current based on the joint angle and the desired torque. The inner loop current controller acts on the current error to command a duty cycle to a buck converter, ultimately exciting the coil.

Fig. 16 shows the experimental results for the position control of the distributed spine with the inner loop current controller. Step position commands for Module 5 are tested while the rest of the modules' references are set to vertical positions. Due to a slight imbalance in the parallel spring mechanism, coil 2 is excited to keep the spine at zero configuration. For the position step command from zero to 1° and zero to 2°, coil 2 current goes zero, and coil 1 is excited. The position control at 2° requires a higher current than that at 1° due to the higher spring torque. The coil currents track well with the references generated from the torque-to-current conversion. However, instability in position control is observed at 3° and beyond, which results in the actuator chattering between two extreme positions.

C. Control Architecture With Inner Loop PI Torque Controller

The inner loop current control is replaced with a torque controller in this architecture, as shown in Fig. 14. The actuator torque is estimated using the lookup table, measured coil current, and position using (20). The PI torque controller acts on the error

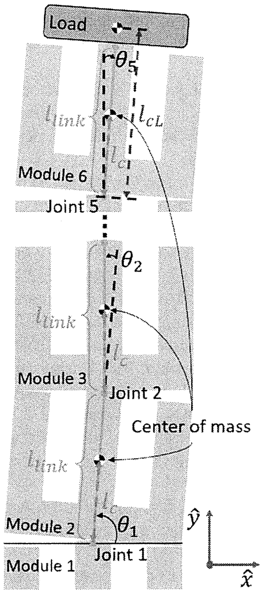

Fig. 20. Load is attached to the top of the spine.

single module [44], not as a part of a spine system. A system-level design methodology for the electromechanical actuator discussed in [52] could result in much higher torque capability, making the response time significantly faster.

E. Load Capability With Position Control

The load capability of the spine is analyzed using the spine's gravitational torque with a load attached on the top, as shown in Fig. 20. The load is added to the spine's gravitational torque presented in [46], considering it is attached to the top module. The gravitational torque with the load is calculated with the Lagrangian formulation using the point mass of each object as

$$g(\theta) = mg \begin{bmatrix} \sigma_5 + \sigma_4 + \sigma_3 + \sigma_2 + \sigma_1 \\ \sigma_4 + \sigma_3 + \sigma_2 + \sigma_1 \\ \sigma_3 + \sigma_2 + \sigma_1 \\ \sigma_2 + \sigma_1 \\ \sigma_1 \end{bmatrix} + m_L g \begin{bmatrix} \sigma_L \\ \sigma_L \\ \sigma_L \\ \sigma_L \\ \sigma_L \end{bmatrix}$$

$$\begin{aligned} \text{where } \sigma_L &= l_{cL}\cos(\theta_1+\theta_2+\theta_3+\theta_4+\theta_5) \\ \sigma_1 &= l_c \cos(\theta_1+\theta_2+\theta_3+\theta_4+\theta_5) \\ \sigma_2 &= (l_{\text{link}} + l_c)\cos(\theta_1+\theta_2+\theta_3+\theta_4) \\ \sigma_3 &= (2l_{\text{link}} + l_c)\cos(\theta_1+\theta_2+\theta_3) \\ \sigma_4 &= (3l_{\text{link}} + l_c)\cos(\theta_1+\theta_2) \\ \sigma_5 &= (4l_{\text{link}} + l_c)\cos\theta_1. \end{aligned} \tag{21}$$

l_{link} is the link length, l_c is the center-of-mass distance from joint, l_{cL} is center-of-mass distance from joint 5 to the load point mass, m is the mass of a single module, and m_L is the load mass. Note that the I-shaped core is ignored for simple analysis. $l_{\text{link}} = 42\,\text{mm}$, $l_c = 22.08$ mm, $l_{cL} = 64$ mm, $m =$ 0.31 kg, $m_L = 0.458$ kg are used for the gravitational torque parameters. Considering the analysis is based on point mass for each object, a 1 lb dumbbell (measured 0.458 kg on a scale) is selected to run the test. Fig. 21 shows the captured moments for the load capability test with position control of the spine from 0° to 4° at all joints. Module 1 experiences the heaviest load because the modules are stacked in the vertical plane. The total mass that Module 1 carries is 2 kg, including five modules and the load.

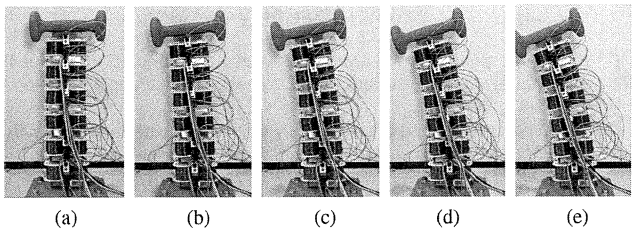

Fig. 21. Captured moments of the distributed spine position control with 1 lb load. (a) 0°. (b) 1°. (c) 2°. (d) 3°. (e) 4°.

TABLE III
INPUT POWER MEASUREMENTS FOR THE SPINE'S JOINT POSITION CONTROL WITH A 0.458 KG LOAD IN STEADY STATE

Each joint position	0°	1°	2°	3°	4°
Input voltage [V]	47.620	47.548	47.764	47.772	47.606
Input current [A]	0.082	0.111	0.134	0.118	0.088
Input power [W]	3.905	5.278	6.400	5.637	4.189

Table III lists the system's input power in a steady state as each joint position is controlled. The joint positions are the relative angular positions from the spine's zero configuration. There is a small input current when all joint positions are zeros, as the position controller corrects the position error caused by a small imbalance of the springs on both sides of each module. Each module requires more current to increase the torque as the position increases from 0° to 2°. However, the input current starts decreasing when the modules rotate from 2° to 4° since the module's torque capability exponentially increases for the same current.

V. CONCLUSION

This article presents a distributed actuator system and compares it to conventional motors. The proposed actuator's mechanical and electrical models are provided and validated with experimental results. A position controller with an inner loop torque controller is proposed for controlling the spine's position. The position control is also validated by the hardware. The proposed actuator's dynamic performance is better than that of regular motors for an articulated spine that requires a small angular flexibility at each joint. Moreover, the proposed actuator's copper loss is much lower than that of the motors.

ACKNOWLEDGMENT

The authors would like to thank the 3M Foundation, Prof. Peter Sauer, and the Power Affiliates Program at the University of Illinois Urbana-Champaign for their support.

[53] Accessed: Apr. 2, 2024. [Online]. Available: https://www.celeramotion.com/applimotion/products/direct-drive-frameless-rotary-motors/torque-plus/omni-plus

[54] Accessed: Apr. 2, 2024. [Online]. Available: https://www.kollmorgen.com/en-us/products/motors/direct-drive/tbm2g-series-frameless

[55] Accessed: Apr. 2, 2024. [Online]. Available: https://www.delta-line.com/cat.pag/frameless-bldc-motors-czk205kzpsxzk520.html

[56] Accessed: Apr. 13, 2024. [Online]. Available: https://sdp-si.com/products/Motors-Gearheads-and-Motion-Control/frameless-brushless-dc-motors/index.php

[57] R. Krishnan, *Switched Reluctance Motor Drives: Modeling, Simulation, Analysis, Design, and Applications.* Boca Raton, FL, USA: CRC Press, 2001.

[58] O. Fröhlich, "Investigations of dynamoelectric machines and electric power transmission and theoretical conclusions therefrom," in *Electrotech Z*, vol. 2. 1881, pp. 134–141.

[59] V. Narayan, "Polynomial approximation of a magnetization curve," *Electron. Theses Diss.*, South Dakota State University, Brookings, SD, USA, 1969.

[60] N. L. Schmitz and D. W. Novotny, *Introductory Electromechanics.* New York, NY, USA: Ronald, 1965.

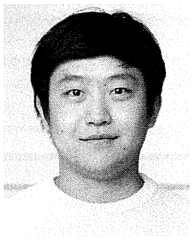

Bonhyun Ku (Student Member, IEEE) received the B.S. degree in electrical engineering in 2016 from the University of Texas at Dallas, Richardson, TX, USA, and the M.S. degree in electrical engineering in 2019 from the University of Illinois at Urbana-Champaign, Urbana, IL, USA, where he is currently working toward the Ph.D. degree in electrical engineering.

From 2015 to 2016, he was an Undergraduate Research Assistant with the Renewable Energy and Vehicular Technology Laboratory, Richardson, TX, USA. He was with Renesas Electronics America, Durham, NC, USA, in 2019 and with Beta Technologies, South Burlington, VT, USA, in 2021. He is currently with Renesas Electronics America as a Senior Applications Engineer. His research interests include robotic actuator design and control, power electronics, and electric machine drives.

Dr. Ku was the recipient of the Kwanjeong Educational Foundation Fellowship for his graduate study in 2017 and was awarded the Third Prize in the 2019 IEEE Energy Conversion Congress and Exposition Student Project Demo Competition.

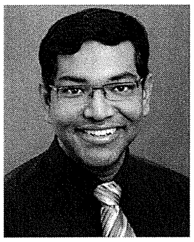

Arijit Banerjee (Senior Member, IEEE) received the B.E. degree from Bengal Engineering and Science University, Shibpur, Howrah, India, in 2005, the M.Tech. degree from the Indian Institute of Technology, Kharagpur, India, in 2007, and the Ph.D. degree from the Massachusetts Institute of Technology, Cambridge, MA, USA, in 2016, all in electrical engineering.

He was with the Power Conversion Systems Group, General Electric Global Research Centre, Bengaluru, India, where he worked on monitoring and diagnostics of electromechanical systems using electrical signatures. From 2006 to 2007, he was a visiting student with the Institute for Power Electronics and Control of Drives, Technische Universität Darmstadt, Darmstadt, Germany, through a German Academic Exchange Service Fellowship. He joined the Department of Electrical and Computer Engineering, University of Illinois, Urbana-Champaign, Urbana, IL, USA, as an Assistant Professor in 2017. He is currently an Associate Professor with the same department. He holds 18 issued patents. His research interests include analysis, design, control, and diagnostics of electromechanical energy conversion systems.

Dr. Banerjee is a Senior Member of the U.S. National Academy of Inventors and an Associate Editor for IEEE TRANSACTIONS ON INDUSTRY APPLICATIONS.